

Impact of Pore Architecture on the Hydroconversion of Long Chain Alkanes over Micro and Mesoporous Catalysts

Laura Vaugon, Annie Finiels, Thomas Cacciaguerra, Vasile Null Hulea, Anne Galarneau, Cindy Aquino, Jean-Pierre Dath, Delphine Minoux, Corine Gerardin, Francois Fajula

▶ **To cite this version:**

Laura Vaugon, Annie Finiels, Thomas Cacciaguerra, Vasile Null Hulea, Anne Galarneau, et al.. Impact of Pore Architecture on the Hydroconversion of Long Chain Alkanes over Micro and Mesoporous Catalysts. Neftekhimiya / Petroleum Chemistry, 2020, 60 (4), pp.479. 10.1134/S0965544120040180 . hal-02565094

HAL Id: hal-02565094
https://hal.science/hal-02565094

Submitted on 3 Dec 2020

HAL is a multi-disciplinary open access archive for the deposit and dissemination of scientific research documents, whether they are published or not. The documents may come from teaching and research institutions in France or abroad, or from public or private research centers.

L'archive ouverte pluridisciplinaire **HAL**, est destinée au dépôt et à la diffusion de documents scientifiques de niveau recherche, publiés ou non, émanant des établissements d'enseignement et de recherche français ou étrangers, des laboratoires publics ou privés.

Impact of Pore Architecture on the Hydroconversion of Long Chain Alkanes over Micro and Mesoporous Catalysts

Laura Vaugon[a], Annie Finiels[a], Thomas Cacciaguerra[a], Vasile Hulea[a], Anne Galarneau[a], Cindy Aquino[b], Jean-Pierre Dath[b], Delphine Minoux[b], Corine Gerardin[a], and François Fajula[a, *]

[a] *Institut Charles Gerhardt, Univ. Montpellier, CNRS, ENSCM, Montpellier, 34095 France*

[b] *Total Research and Technology Feluy, Feluy, 7181 Belgium*

**e-mail: ffajula@enscm.fr*

Received November 15, 2019; revised December 9, 2019; accepted December 10, 2019

Abstract—*n*-Hexadecane hydroconversion has been investigated in a series of bifunctionnal metal/acid catalysts featuring distinct well-defined pore architectures. The acidic components were prepared from dealuminated Y zeolites with Si/Al of 15 and 30 post treated in alkaline medium to generate ordered or non-ordered secondary networks of mesopores and from aluminated ordered mesoporous materials MCM-41, MCM-48, KIT-6 type materials and amorphous silica gel. Activity relates linearly to the strength and number of strong Brönsted acid sites, while selectivity, more precisely the yield in isomerization products, scales directly with the mesopore volume of the catalyst. The architecture of the mesoporous network, namely the ordering, interconnectivity, homogeneity of the mesopores, affects little catalytst behavior. Confrontation of catalytic data with diffusion measurements suggests the existence of an optimal mesopore size above which the number of strong Brönsted sites and the mesopore volume are the only parameters governing catalytic performance.

Keywords: hydroisomerization, *n*-hexadecane, mesoporous zeolites, MCM-41, MCM-48, KIT-6, diffusion

DOI: 10.1134/S0965544120040180

INTRODUCTION

Hydroconversion (HDC) processes such as hydrocracking and hydroisomerization play a key role in modern refineries as they allow the transformation of a wide range of feed stocks into high value products [1]. Hydroconversion catalysts combine two functions, an acidic component consisting, on the one hand, of an amorphous or crystalline oxide and, on the other hand, of a hydrogenation-dehydrogenation component which formulation depends on the nature and composition of the feed to be converted and the experimental conditions. Under ideal hydroconversion conditions, when the hydrogenating/dehydrogenating function is not limiting, it has been demonstrated for long that product selectivity is strongly impacted by the porosity of the catalysts [2] while it hardly depends on acidity [3]. This can be easily understood since selective hydroconversion processes, which involve multi-site and multi-step catalytic cycles, require fast hydrogenation and desorption of highly reactive olefinic intermediates to prevent consecutive secondary non-selective reactions.

The influence of pore architecture on product selectivity during hydrocracking, where the production of high value middle distillates is targeted, is well illustrated in several papers [4–7]. For instance, in the case of the conversion of a model phenantrene molecule over zeolitic catalysts, at a given temperature and total conversion, the yield of the most valuable intermediate hydrocracked products scales almost linearly with the pore size, or the pore volume, of the catalyst [6]. The results were rationalized using a very simple model based on the confinement theory introduced by Derouane et al. [8–10].

In the processing of a real feedstock, consisting in a mixture of straight run VGO, aromatic extract and heavy coker gas oil, over a composite $NiMo/Al_2O_3$/Faujasite catalyst, it was shown that the selectivity in middle distillate increased with the mesopore volume generated by a dissolution/reconstruction treatment of the acidic faujasite [7]. In terms of productivity, however, optimal middle distillate yields were obtained with the catalysts where the zeolite component has been only moderately modified which feature the highest acidity.

Hydroisomerization of long chain alkanes is also a domain of strong academic and industrial concern as this reaction is at the basis of very important conversion technologies aiming at improving the cetane number of diesel and jet-fuels and the cold flow properties of fuels and lubricants. The domain has been periodically reviewed [11–16]. Most efforts have been paid to develop catalytic systems and experimental conditions aiming at optimizing the yields of isomers

while reducing secondary cracking reactions. In that respect a large body of literature has been produced to delineate the ideal characteristics for crystalline and amorphous acidic hydroisomerization catalyst components. It turns out that, when the acidic and metallic functions are well balanced, aside the structural type [17–22], the crystal size and morphology [23, 24] and the nature of the acid sites [25–27] of the zeolite component, the textural features, namely the presence of a secondary network of mesopores, dramatically impacts the isomer selectivity [28–32]. In all cases, selectivity improvement has been related to mass transport enhancement, favoring desorption of the primary isomer products.

In order to better apprehend, and possibly quantify, the beneficial effect of the presence of mesopores on the hydroisomerization selectivity of HDC catalysts, we prepared a series of model catalysts featuring unique and well-defined textural features and pore architectures. The materials have been characterized and their catalytic behavior compared under the very same experimental conditions in the transformation of *n*-hexadecane.

EXPERIMENTAL

Materials

Zeolite materials. Zeolite-based catalysts were produced starting from two parent materials obtained from Zeolyst International, namely CBV 720 (FAU type, Si/Al = 15, hereafter HY-15) and CBV 760 (FAU type, Si/Al = 28.4, hereafter HY-30). Both materials have been prepared by the supplier by steam dealumination and acid leaching of a parent aluminium-rich faujasite. The pore architecture of the two parent samples has been modified by using various treatments in alkaline medium in order to increase and re-engineer their secondary mesoporous network.

HY-30 meso-d was obtained by submitting the parent HY-30 to a desilication treatment with 0.05 M NaOH solution at room temperature for 15 min as described in ref [28].

HY-15 meso-r and HY-30 meso-r were produced by a desilication/reconstruction protocol in the presence of cetyltrimetylammonium bromide (CTAB) surfactant [32–39] by reaction for 20 h at 150°C with a 0.09 M solution of tetramethyl ammonium hydroxide (TMAOH) for HY-15 meso-r, and for 1 h at 150°C with a 0.07 M solution of TMAOH for HY-30 meso-r [40, 41].

The as-synthezized materials were oven dried overnight at 80°C and finally calcined at 550°C for 8 h under air flow. The material HY-30 meso-d is obtained as Na^+ form and requires a cation-exchange (see below) to provide H^+ form. HY-15 meso-r and HY-30 meso-r are directly produced under H^+ form.

Mesosporous materials. LiChrospher 60 has been given by Merck and consists in 12 μm silica-gel particles with a mesopore network with pore openings centered at 6 nm.

A large-pore silica material with cubic I_{a3d} symmetry, named KIT-6 [42] was synthesized by reaction in teflon-lined autoclave at 130°C for 24 h of a mixture of triblock-copolymer Pluronic P123 ($EO_{20}PO_{70}EO_{20}$, Aldrich) and butanol as structuring agents, tetraethylorthosilicate (TEOS) as silicon source and HCl, after an aging of 24 h at 35°C [43]. The molar composition of the starting gel was: 1 SiO_2/0.017 P123/1.9 HCl/1.3 butanol/194 H_2O. The slurry was then filtered and washed rapidly with a HCl/EtOH solution before to be dried at 100°C for 24 h and calcined at 550°C for 8 h.

The MCM-41 sample (Al-MCM-41, Si/Al = 15) was synthesized using Aerosil 200 as silica source, CTAB as surfactant, NaOH, deionized water in molar composition: 1 SiO_2/0.1 CTAB/0.25 NaOH/0.066 $NaAlO_2$ / 20 H_2O [44, 45]. After dissolution of CTAB in water in presence of NaOH and $NaAlO_2$ at 50°C, silica is added progressively and the suspension is stirred for 1 h. The slurry is then put in autoclave for 20 h in static condition at 115°C. The resulting slurry is then filtered and washed with water until neutral pH, dried at 80°C overnight and calcined at 550°C for 8 h.

Silica MCM-48 was synthesized by following the procedure recommended by Galarneau et al. [46] from powdered silica (Aerosil 200), CTAB, NaOH and deionized water in the following molar composition: 1 SiO_2/0.38 NaOH/0.175 CTAB/120 H_2O. After dissolution of CTAB in water in the presence of NaOH at 50°C, silica was added progressively and the suspension was stirred for 2 h. The slurry was then put in autoclave at 150°C for 15 h without stirring. The solid precipitate was then filtered, not washed, and dried at 80°C overnight. The resulting powder was then subjected to two successive hydrothermal post-treatments in deionised water at 130°C for 6 h. Between each post-treatment, the suspension was filtered, not washed, and dried at 80°C overnight. After the second post-treatment, the slurry was filtered and washed until neutral pH before being dried at 80°C overnight and calcined at 550°C for 8 h. This procedure is important in order to improve the thermal, chemical and mechanical stabilities of MCM-48 [46].

Alumination of the surface of the mesoporous silica materials. In order to generate acid sites, aluminium species were grafted at the surface of the siliceous mesoporous silica materials MCM-48, KIT-6 and LiChrospher according to two procedures.

MCM-48 was aluminated according to a method similar to that proposed by Lengo et al. [31, 47] using $Al(O\text{-}sec\text{-}C_4H_9)_3$ as Al source. The suspension of MCM-48 in 150 mL of dry toluene ($H_2O < 0.002\%$) was contacted with triethylamine and Al(O-*sec*-

Table 1. Characteristics of the different catalysts

Sample no.	Catalyst	Si/Al, mol	Pt, wt %	V_{Total}, mL/g	V_{micro}, mL/g	V_{meso}, mL/g	D_{meso}, nm	Acidity, mmol/g	Iso C_{16} yield[4], wt %
1	HY-15	15	0.5	0.43	0.37	0.06	5-50	0.33	29.4
2	HY-15 meso-r	13	0.43	0.59	0.24	0.35	3.3/5-50	0.27	49.3
3	HY-30[1]	28.4	0.40	0.50	0.23	0.27	5–50	0.23	45
4	HY-30[2]	28.4	2	0.50	0.23	0.27	5–50	0.22	46.1
5	HY-30 meso-d	23	0.5	0.52	0.15	0.37	3.3/5–50	0.18	58
6	HY-30 meso-r	22	0.46	0.58	0.24	0.35	3.9	0.18	55
7	MCM-41	5	0.5	0.65	–	0.65	3.5	0.09	71.1
8[3]	MCM-48	5	0.39	0.54	–	0.54	3.3	0.22	70.1
9	LiChrospher	5	0.45	0.46	–	0.46	5–10	0.10	66
10	KIT-6	5	0.35	0.80	–	0.71	7.1	0.11	71.4

[1,2]HY-30 has been loaded with 2 different amounts of Pt, [3]from ref [31], [4]maximum isomerization C16 yield.

$C_4H_9)_3$ at 85°C for 6 h. The solid recovered by filtration was washed with toluene and then suspended in ethanol containing the stoichiometric amount of water corresponding to the amount needed for a complete hydrolysis of the AlOR groups. The suspension was stirred for 24 h at 25°C. The final solid was washed with ethanol, oven dried and calcined in flowing air at 400°C for 2 h and 550°C for 4 h.

Surface alumination of KIT-6 and LiChrospher was achieved according to the procedure described by Luan et al. [48, 49]. The silica materials were suspended under stirring in an aqueous solution containing sodium aluminate (corresponding to a molar ratio Si/Al = 5) for 15 h, at room temperature. The solid sample was recovered by filtration, washed with water, dried at 80°C in air and calcined for 6 h in air at 550°C.

The aluminated mesoporous materials KIT-6 and LiChrospher, MCM-41 and desilicated zeolite HY-30 meso-d were subjected to a cation-exchange treatment. 6.3 g of materials were poured in 630 mL of ethanol solution containing NH_4NO_3 (0.1 M). The suspension was maintained under reflux for 1 h, before being filtered without washing. The post-treatment was repeated 3 times. After the third post-treatment the powder was washed with 200 mL ethanol 3 times, dried at 80°C overnight and then calcined at 450°C for 6 h.

Catalysts preparation. Bifunctional catalysts were prepared by loading 0.3 to 2 wt % platinum (Table 1) on the acidic supports by using the incipient wetness method at room temperature with hexachloroplatinic acid hexahydrate as metal source [28, 31]. The solids were oven dried at 80°C for 2 h, then at 120°C for 12 h and finally calcined (ramp of 2°C/min) at 550°C in flowing air for 8 h. The catalysts were shaped into 250–425 μm particles obtained by compressing the powder under two tons, crushing and sieving.

Methods

Physicochemical characterization. X-ray diffraction (XRD) patterns were collected using a Bruker D8 Advance diffractometer with a Bragg-Brentano geometry, equipped with a Bruker Lynx Eye detector and using CuK_α radiation and a Ni filter. XRD patterns were recorded in the range 4°–50° (2θ) to identify zeolite peaks and in the range 0.4°–6° to characterize mesostructure architecture. Textural properties of the materials were determined from N_2 adsorption-desorption isotherms at 77 K recorded on Micromeritics ASAP 2010 apparatus. The Broekhoff and De Boer (BdB) method was applied to the N_2 desorption isotherm to calculate mesopore diameters, as previously recommended for MCM-41 materials [50]. Micropore volumes were evaluated by the corrected t-plot method drawn in the domain $0.005 < p/p_0 < 0.18$ [51]. Total pore volumes were calculated from the amount of nitrogen adsorbed at a relative pressure p/p_0 of 0.95 for zeolites and desilicated zeolites and at the end of the mesopore filling for mesoporous materials and transformed zeolites using surfactants.

Transmission electron microscopy (TEM) images were recorded using a JEOL 1200 EX2 microscope operating at 100 kV. SEM images and EDX elemental analyses were performed using a FET Quanta 200F microscope operated at 15 kV.

The amount of strong acid sites was determined by temperature-programmed desorption of ammonia (NH_3-TPD) using an AUTOCHEM 2910 apparatus from Micromeretics [31]. The samples were pretreated at 550°C under airflow (30 mL/min) for 10 min. After cooling down to 100°C, the surface was saturated with ammonia (45 mL/min) using a mixture NH_3/He (5% NH_3) for 30 min. Physisorbed NH_3 was removed by evacuation at 120°C for 30 min in a dry helium stream

(25 mL/min). The ammonia desorption was carried out in a helium stream (25 mL/min) at a heating rate of 10°C/min up to 600°C. The amount of desorbed ammonia was monitored with a thermal conductivity detector. Under these conditions ammonia desorbs in two steps: a low temperature desorption step (with a peak maximum at around 200°C) and a high temperature desorption step with a maximum desorption temperature at around 400°C. In the following the amount of strong acid sites has been calculated from the area of the high temperature desorption peak. The nature of the acid sites has been monitored by studying the interactions of the surface with perdeuterated acetonitrile by infrared spectroscopy using a Bruker Equinox 55 spectrometer in the transmission mode on self-supporting wafers. The samples (20–40 mg) were activated under vacuum at 450°C for 12 h, and acetonitrile (1.5 Torr) was adsorbed at room temperature. Spectra were recorded after evacuation at increasing temperatures, up to 100°C.

Catalytic testing. Hydroconversion of *n*-hexadecane (n-C_{16}, 99.9% purity, Sigma Aldrich) was studied in a downstream fixed-bed continuous flow reactor (6 mm ID) using 1–1.3 g of catalyst shaped into 250–425 μm particles [28, 31]. The catalyst pre-calcined at 550°C in flowing air (see above) was reduced in situ in flowing hydrogen (3 NL/h) at 400°C for 12 h (heating rate 10°C/min). The hydrocarbon was pumped at a rate allowing a weight hourly space velocity (WHSV) comprised between 1 and 3 h^{-1} into a vaporization chamber preheated at 130°C and mixed with hydrogen with a molar H_2/hydrocarbon ratio of 4 at a total pressure of 20 atm. The reaction temperature was varied between 220 and 320°C. After catalyst testing, the reactor was depressurized under hydrogen flow at 300°C. After 3 h the flow was switched to nitrogen and the temperature decreased to room temperature.

Reaction products were analyzed by gas chromatography using a fast-GC Agilent 7890A chromatograph operated with a GC OpenLAB software. An apolar column was used (100% dimethylpolysiloxane, 20 m × 100 μm × 0.4 μm, Agilent 127-0123). Detection of the products was achieved by FID.

Light hydrocarbons, up to C_9, were analyzed on line while the liquid fractions were collected and analyzed separately. The total conversion was defined as $(1 - F_{\text{hc out}}/F_{\text{hc in}}) \times 100$, where F_{hc} is the molar n-C_{16} hydrocarbon flow. Product yields are reported on a carbon, or weight, basis. Hydroisomerization products were grouped into three lumps (mono, di and tri branched). Hydrocracking products were grouped by carbon number. In all runs, carbon balances higher than 98% were achieved.

RESULTS AND DISCUSSION

Materials

Texture. Nitrogen adsorption isotherms and characteristic TEM images of the catalysts are presented in Figs. 1–4. The starting materials, HY-15 and HY-30 feature the isotherm shape typical for steam dealuminated zeolites characterized by a flat hysteresis loop in the high pressure range. Such a hysteresis is indicative of the presence of mesopores with a broad distribution of sizes in the range from 5 to higher than 50 nm. The mesopores are distributed over the whole crystal (Fig. 3). The sharp closure of the hysteresis loop at a relative pressure $p/p_0 = 0.43$ is characteristic of cavitation phenomenon and suggests the presence of cavities entrapped in the microporous zeolitic network [52]. After the alkaline treatments HY-30 meso-d, HY-30 meso-r, HY-15 meso-r (samples 2, 5, 6, Table 1), the micropore volume of the samples decreased while their mesopore volume increased to a larger extent as a result of the desilication reaction, evidenced by the increase of the Si/Al ratios. The architecture of the new mesopores thus created significantly differs depending on the conditions of the alkaline treatment. The mechanism and the outcome of the desilication of HY-30 by dilute soda in the absence of surfactant (HY-30 meso-d) have been investigated using combined TEM and electron tomography and described in detail in ref [28]. Base leached crystals contain unaffected microporous domains, as in the starting zeolite, while the density and the size of the mesopores have been slightly increased. Remarkably, the alkaline dissolution generated a new network of small mesopores, with a diameter in the range 2–10 nm, interconnected to the larger mesopores or to the surface of the crystals. HY-30 meso-d features therefore a trimodal porosity, with the structural micropores and two distinct networks of mesopores, 2–10 and 5–50 nm, both with non uniform distributions of sizes.

The mesopore architecture of HY-15 meso-r and HY-30-meso-r was somewhat different since the presence of CTAB surfactant in the reaction medium and the experimental conditions allowed the reconstruction of the dissolved matter into ordered silicoaluminate mesoporous structures intimately embedded in the zeolite crystal [39–41, 52, 53]. The presence of mesopores with a narrow distribution of sizes at 3.9 nm is evidenced from the sorption isotherm by the adsorption step at $p/p_0 = 0.37$. The isotherm also reveals that crystal reconstruction has resulted in the disappearance of the large mesopores of 5–50 nm present in the starting material. In the TEM images, we can see that these ordered mesopores are distributed over the whole crystal together with nanodomains of a few hundreds of nm of crystalline zeolite. HY-15 meso-r and HY-30-meso-r can be therefore regarded as composite materials with hierarchical porosity, consisting of zeolitic and mesostructured

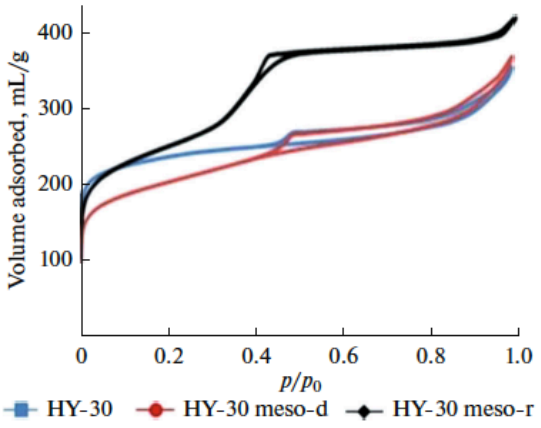


Fig. 1. Nitrogen sorption isotherms at 77 K of materials derived from HY-30.

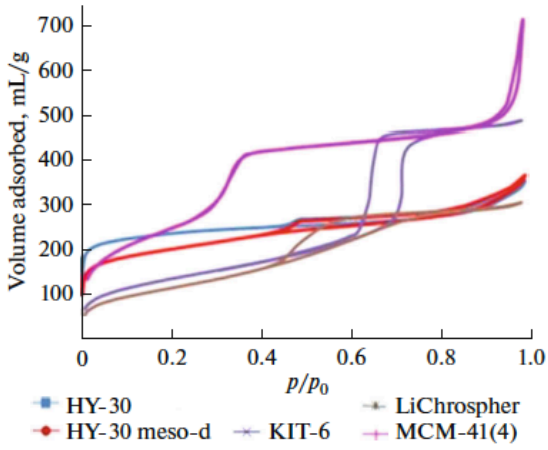


Fig. 2. Nitrogen sorption isotherms at 77 K of zeolitic and mesoporous materials.

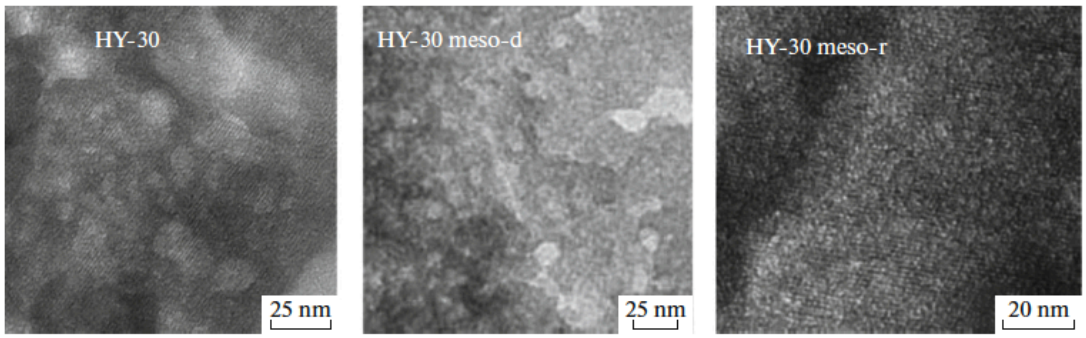


Fig. 3. TEM images of zeolitic materials.

nanodomains as reported for the first time by Goto et al. [33] and further by others [40, 53–56].

The pore architecture of the purely mesoporous materials was more straightforward. MCM-48 and KIT-6 feature a cubic Ia3d symmetry with a bicontinuous gyroid mesostructure. Their pores are 3D interconnected with a very narrow distribution of sizes (Fig. 4) centered at 3.7 and 7.2 nm for MCM-48 [31] and KIT-6, respectively, derived from the position of the steep adsorption step of the isotherms. TEM images (Fig. 4) reveal moreover that the pores are very well ordered over the whole particles. After alumination by aluminium alkoxide, MCM-48 features a slight decrease in mesopore diameter of 3.5 nm.

MCM-41 exhibits an ordered one directional (1 D) system of pores in line with the hexagonal P6mm symmetry of the mesophase with uniform pore diameters of 3.5 nm. Similar to the cubic systems, TEM reveals the presence of pores in all the volume of the particles (Fig. 4).

LiChrospher is produced by the aggregation of 12 nm silica-gel particles (Fig. 4) producing a 3D network of interconnected mesopores with a distribution of sizes (5–10 nm) centered at 6 nm (cavities around 6.5 nm and constrictions around 4.5 nm diameter).

Pore volumes of the different solids are listed in Table 1.

Acidity. All materials exhibited similar TPD profiles, with varying densities of acid sites (Table 1). MCM-41, KIT-6 and LiChrospher features around 0.1 mmol/g of strong acid sites, MCM-48 and HY-30 based catalyst around 0.2 mmol/g and HY-15 based catalysts around 0.3 mmol/g. The fact that similar desorption profiles are obtained is consistent with the high basic strength of NH_3 ($pK_b = 4.75$). Differences in acid strength can be therefore hardly seen. The method is however widely accepted to dose the total number of acid sites at the surface of solids due to its simplicity and to the good precision of the data recorded. In order to determine the nature of the acid sites, and to tentatively evidence differences in acid

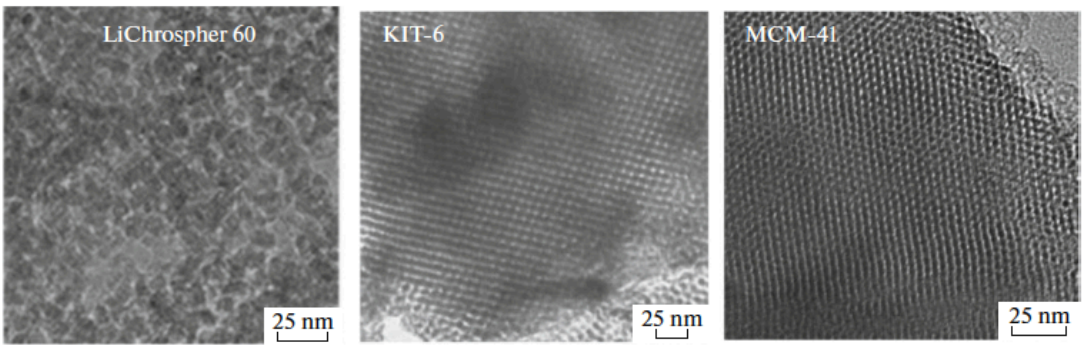


Fig. 4. TEM images of mesoporous materials.

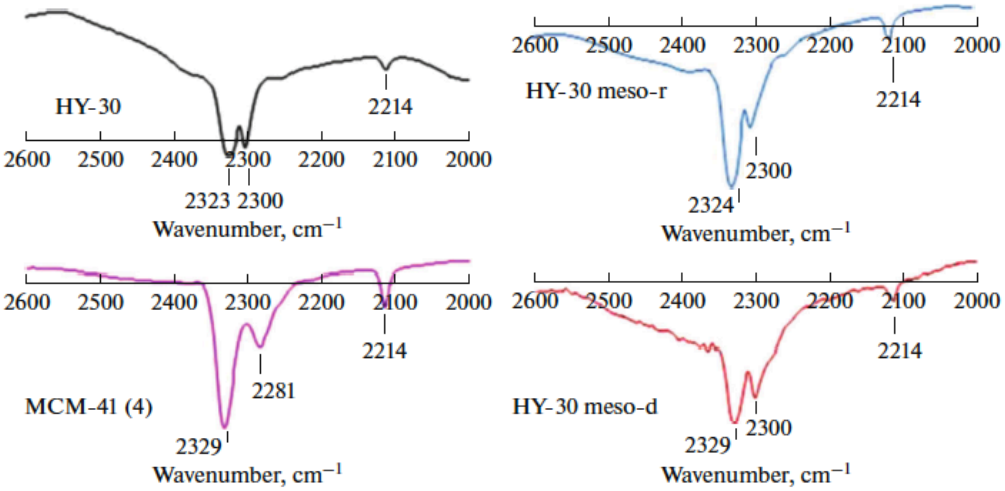


Fig. 5. Infrared spectra in the region of CN and CD vibrations for perdeuterated acetonitrile adsorbed on various catalysts after desorption at 50°C.

strengths, we used IR spectroscopy of adsorbed perdeuterated acetonitrile. Acetonitrile is a weak base ($pK_b = -11$), it doses only the strongest acid sites and allows to discriminate between Lewis and Brönsted sites [57–61]. After dosing 1.5 torr of acetonitrile at room temperature and desorbing the sample at 50°C for 15 min, characteristic signals for acetonitrile adsorbed on Lewis sites (2323–2329 cm^{-1}) and on Brönsted sites (2280–2300 cm^{-1}) were detected (Fig. 5). (The signal at 2115 cm^{-1} corresponds to the symmetric C–D stretching mode of chemisorbed acetonitrile).

Though the acidity of the surface of the different materials was qualitatively similar, with however larger proportions of Lewis sites on the modified zeolites and on the aluminated mesoporous catalysts than on the starting HY-30 zeolite (Fig. 5), it can be noted that the position of the maximum of the peak associated to Brönsted sites is slightly shifted towards lower wavenumbers in the case of mesoporous materials, suggesting a lower strength of their Brönsted sites (Table 2). Among purely mesoporous materials, MCM-48 aluminated by the aluminium alkoxide route features the highest strength of Brönsted sites and the highest number of strong acid sites (Table 1).

Catalytic activity. The activity of the catalysts for the conversion of *n*-hexadecane was evaluated under a total pressure of 20 atm. with a molar H_2/hydrocarbon ratio of 4 in the temperature range 220–320°C. Activity versus temperature curves are shown in Fig. 6. Arrhenius plots drawn for conversion levels lower than 30% allowed to calculate apparent activation energies in the range 120–140 kJ/mol for all catalysts. Such values are characteristic for a bifunctional mechanism of alkane hydroconversion free from mass transport constraints [62].

Table 2. Position of the bands characteristic of Brönsted and Lewis acidity determined by IR of adsorbed acetonitrile

Sample no.	Catalyst	Band position Lewis, cm^{-1}	Band position Brönsted, cm^{-1}
3	HY-30[1]	2323	2300
5	HY-30 meso-d	2329	2300
6	HY-30 meso-r	2324	2300
7	MCM-41	2329	2281
8[1]	MCM-48	2323	2290

[1]From ref [31].

As reported previously [28, 31], under the experimental conditions used, no loss of activity nor selectivity was observed under long lasting and duplicate runs. Used catalysts featured a broad distribution of metal particles, with large particles (>15 nm) coexisting with a high population of small (<3 nm, 50% of the particles detected) metal clusters. In terms of selectivity all catalysts demonstrated the behavior of ideal bifunctional catalysts [63, 64]. The primary products formed were monobranched isomers. Increasing the conversion led to the production of multibranched isomers and ultimately cracking products formed above *ca* 40% total conversion (Fig. 7).

In terms of activity however large differences were revealed (Fig. 5). The catalysts with the highest strength of acidity, zeolite-based catalysts and MCM-48, demonstrated a higher activity than the other purely mesoporous catalysts with a temperature 40°C lower. Such a situation results from a difference in acid strength of the various solids, as evidenced by IR spectroscopy of adsorbed acetonitrile. Interestingly, for the zeolite-based catalysts and MCM-48, a unique linear relationship (Fig. 8) can be established between the reaction rate of *n*-hexadecane transformation at 230°C and the amount of strong acid sites measured by ammonia TPD. This unique correlation indicates that the acid sites present on these catalysts are of the same nature and strength as those present in the starting zeolite and are not modified by the alkaline treatments performed using or not surfactants.

Another difference concerning the maximum yields of isomer products was also clearly evidenced (Fig. 7 and Table 1). All materials (except the parent zeolites HY-30 and HY-15) demonstrated high selectivities in isomerization, with maximum isomer yields reached at very high total conversion (80–90%) but with however definite differences between the catalysts. While this maximum was at 30% for HY-15 at *ca* 50% for HY-30 and 55–58% for the modified zeolites, it increased to 70% for the purely mesoporous catalysts. This isomer yield gain is consistent with a faster desorption of the primary products of the reaction favored by the increase of the mesoporosity of the catalysts as previously reported [28–32]. Our data allows however a further analysis of the phenomenon. They clearly suggest that the mesopore architecture (homogeneity of sizes or interconnectivity) of the catalysts has little, if any, influence on selectivity, more precisely on the maximum isomer yields. For instance, despite a totally different mesoporous network, HY-30 meso-d and HY-30 meso-r (multimodal and broad distribution of mesopores sizes for HY-30 meso-d and monomodal with a very narrow mesopore size distribution for HY-30 meso-r) lead to equivalent amounts of isomers. Similarly, the isomer yields obtained with KIT-6, MCM-48 and LiChrospher (3 D network of mesopores) and MCM-41 (1 D network of mesopores) are identical. The key parameter governing selectivity in the hydroisomerization of *n*-hexadecane under the conditions of our study is definitely the mesopore volume of the catalysts, regardless of the architecture of the porous network, as shown in Fig. 9.

Relationship between mass transport and selectivity. In related works from our group, the mass transport properties of most porous supports used in the present study have been determined experimentally. It is therefore appealing to correlate the diffusion data with the catalysis results.

The effective diffusion coefficients for n-hexane at room temperature in HY-15, HY-15 meso-r and MCM-41 have been measured using PFG NMR spectroscopy [65, 66].

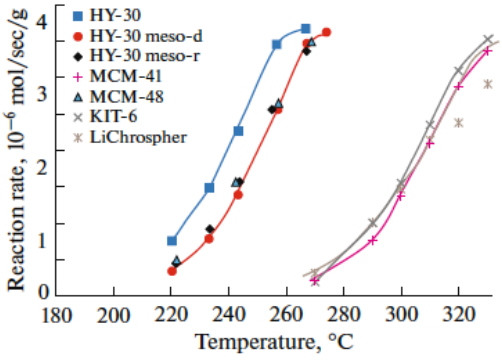


Fig. 6. Reaction rate of *n*-hexadecane conversion as a function of reaction temperature.

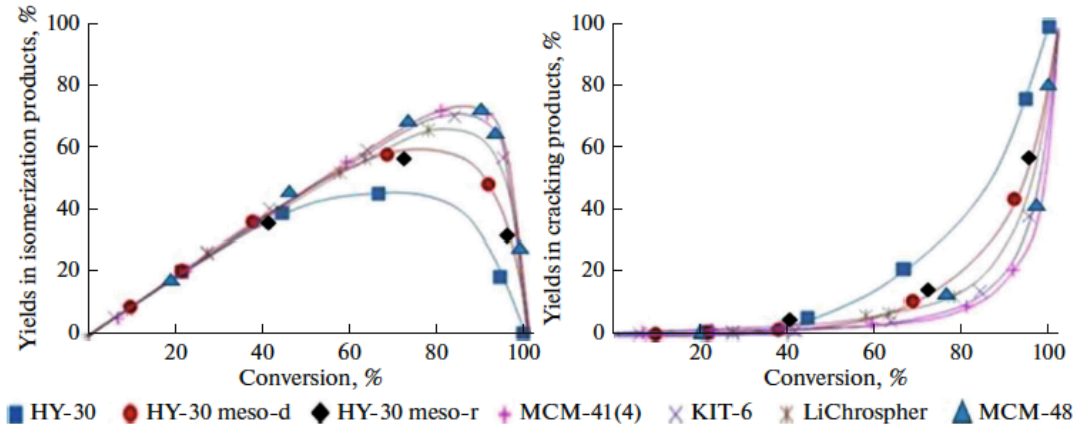


Fig. 7. Yields in isomerization and cracked products as a function of total *n*-hexadecane conversion.

On the other hand mass transport properties of MCM-41, LiChrospher, KIT-6 and MCM-48 have been determined from chromatographic measurements performed using dibutylphatalate as solute [67]. Data were obtained by employing the Van Deemter equation (H = A + B/u +Cu), which correlates the plate height (H, mm) of a chromatography column with the linear velocity (u, in cm/min, proportional to the flow rate F, in mL/min) of a solute. In this equation, the term A represents the mass transfer in the macroporous network and is independent of flow rate, the B term is the lateral diffusion of the solute in the liquid (mainly dependent of the solute) and the C term represents the mass transfer in the mesoporous network of the sorbent particles [68, 69].

Galarneau et al. [70] showed that the chromatographic and the NMR data are correlated by the equation:

$$D_{\text{eff}} = (C_{ms}/C)\,d_p^2 = A(1/C) = B(t/m)(D/\sigma), \quad (1)$$

where C_{ms} is the mass transfer flow, D the mesopore diameter, d_{p} the particle size, σ the molecule diameter, m the pore geometrical factor ($m = 2$ for a cylindrical pore, $m = 3$ for a spherical pore) and t the connecting factor ($t = 1$ for non connected pores, $t = 1.45$ for connected pores).

Diffusion coefficients for n-hexane and the resulting molecular diffusion rates are listed in Table 3. The impact of the presence of mesopores in zeolite crystals and of the pore architecture—size and dimensionality—of mesoporous materials is distinctly highlighted.

In Fig. 10 we have plotted the maximum yields of isomer products formed during the hydroconversion of *n*-hexadecane versus the effective diffusion coefficients (left) and molecular diffusion rates (right) for typical porous supports used in the present study. Both

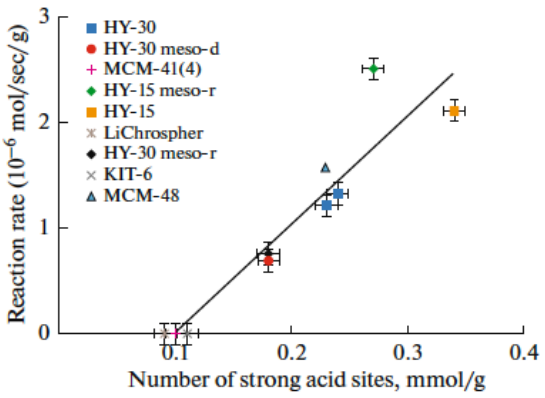


Fig. 8. Correlation between the rate of *n*-hexadecane transformation at 230°C and the number of strong acid sites measured by ammonia TPD.

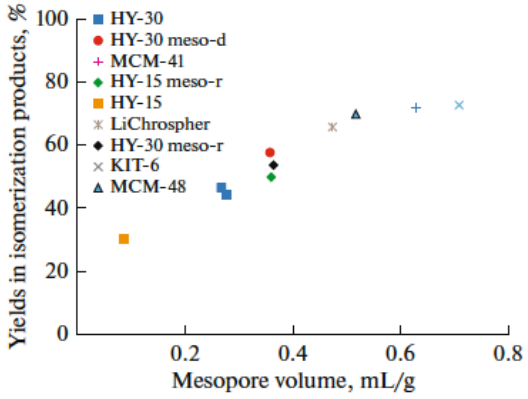


Fig. 9. Maximum isomer yields in the hydroconversion of *n*-hexadecane as a function of the mesopore volume of the catalysts.

representations emphasize a steep increase in isomer yields upon generation of an additional mesoporous network of pores in zeolite crystals and a constant value of the isomer yield over the mesoporous catalysts, regardless of the geometry of their porous network and despite a wide variation of the transport kinetics.

Several semi-empirical models have been proposed to correlate catalytic performance and mass transfer in porous systems. Models integrating pore characteristics such as pore size, shape, tortuosity or connectivity [1, 6, 10, 71–73] show that diffusion rates increase continuously with pore diameter. Recently the group of Tallarek [74] has proposed an equation to express the diffusive hindrance factor (H) which quantifies the degree to which diffusion through a mesoporous material (D_{eff}) is hindered compared with diffusion in the bulk liquid (D_m) as a function of λ, the ratio between the solute size and the pore size ($H(\lambda) = D_{eff}/D_m$). This equation allows to establish quantitative morphology/transport relationships in separation processes and shows that, for a solute confined in mesopores, diffusion rate sharply increases with mesopore size up to a value corresponding to *ca* 10 times the size of the solute. Above this threshold, diffusion rate is a single linear function of mesopore volume, but at the expense of loading capacity.

Since reactivity results from the interaction of the moving molecule with the active sites, catalytic performance will require maximum interaction with the surface, which is achieved in very small pores generating high surface area. These opposite trends imply that a compromise between mass transfer and reactivity has to be found in designing optimal catalysts. Such a compromise has been proposed to correspond to materials featuring pore diameters equivalent to 5–7 times the size of the reactant molecules [70]. Interestingly this value is close to that proposed by Tallarek [74] for separation applications.

Table 3. Effective diffusion coefficients (D_{eff}) and molecular diffusion rates (r) for n-hexane at room temperature on porous supports

Material	D_{eff}, 10^{-10} m^2/s	r, μm/s
HY-15	2.2[1]	0.36
HY-15 meso-r	14[1]	0.92
MCM-41	120[1]	2.68
MCM-48	150[2]	3.0
LiChrospher	200[2]	3.46
KIT-6	300[2]	4.24

[1]Measured by PFG NMR, [2]calculated using Eq. (1).

It is remarkable to note that a ratio of 7 would correspond to a system of cylindrical pores in which the same amount of molecules stand in the adsorbed state and in the mobile phase inside the pore.

If we refer to the case of the hydroconversion of *n*-hexadecane, and taking a value of 0.53 nm for the kinetic diameter of mono-branched alkanes [75], the above hypothesis would predict an optimun pore size of *ca* 3.5 nm, fully in line with our observations.

CONCLUSION

Hydroconversion of *n*-hexadecane over a series of model bifunctional catalysts featuring acidic components with well-defined distinct porous architectures allows us to bring new insights into the role of porosity on catalytic performance. Creation, or increasing the

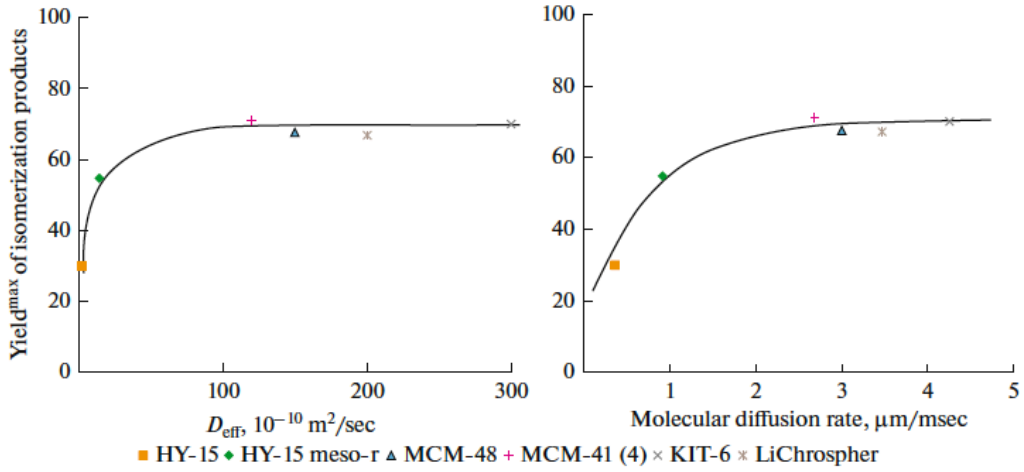


Fig. 10. Correlation between the maximum *n*-hexadecane isomer yield and the diffusion characteristics of typical porous supports used in the study.

volume of mespores in zeolitic materials leads, as expected, to a significant increase of the isomerization selectivity by favoring the rapid desorption of the primary products. For a given mesopore volume, the structuration or the ordering of the mesoporous network does not bring additional benefit in terms of catalyst efficiency. In the case of purely mesoporous materials, the isomer selectivity is also a function of the mesopore volume, and, here again, the pore size, shape and connectivity do not influence catalytic outcome while, at the same time, these factors have a strong impact on diffusion kinetics. Since catalytic processes require both fast mass transport—favored in larger pores—and interaction with a large active surface—favored in small pores—it is suggested that an optimum pore size, set at 5–7 times the size of the reactant molecules, would result in optimal catalytic performance. Such an optimal pore diameter would be at *ca* 3.5 nm for the hydroconversion of *n*-hexadecane and corresponds to the pore sizes of the MCM-41 and MCM-48 type materials. Larger pore sizes, up to 7 nm for KIT-6 for instance, allow faster diffusion kinetics but do not bring additional selectivity benefit.

Our data show moreover that activity is a linear function of the number of strong acid sites. The use of different methods for the alumination of mesoporous catalysts, by direct synthesis for MCM-41, by alumination using alkoxide in organic medium for MCM-48 or by deposition of alumina in aqueous medium for KIT-6 and LiChrospher reveals dramatic differences in the strength of the acid sites generated. The alkoxide route produces acid sites with a strength comparable to that of zeolites.

In spite of its simplicity, the concept of optimal pore size should prove very useful for the selection of optimal catalysts in many catalytic processes.

ACKNOWLEDGMENTS

The authors thank Total S.A. for fruitful discussions and financial support. L.V. thanks ANRT and Total for a grant. The authors wish to acknowledge the support from the Chemistry Plateform of Campus in Montpellier (Plateform MEA University Montpellier), on which TEM and EDS experiments have been performed.

REFERENCES

1. W. Vermeiren, and J. P. Gilson, Top. Catal. **52**, 1131 (2009).
2. E. Ruckenstein and M.C. Tsai, AIChE J. **27**, 697 (1981).
3. E. Benazzi, L. Leite, N. Marchal-George, et al., J. Catal. **217**, 376 (2003).
4. K. Sato, Y. Nishimura, H. Shimada, Catal. Lett. **60**, 83 (1999).
5. K. Sato, Y. Nishimura, K. Honna, et al., J. Catal. **200**, 288 (2001).
6. H. Toulhoat, P. Raybaud, E. Benazzi, J. Catal. **221**, 500 (2004).
7. M. O. Kazakova, K. A. Nadeina, I. G. Danilova, et al., Catal. Today **305**, 117 (2018).
8. E. G. Derouane, J. M. André, and A. A. Lucas, J. Catal. **110**, 58 (1988).
9. I. Derijcke, J. P. Vigneron, Ph. Lambin, A. A. Lucas, and E. G. Derouane, J. Chem. Phys. **94**, 4620 (1991).
10. E. G. Derouane, J. Mol. Catal., A **134**, 29 (1998).
11. H. Deldari, Appl. Catal., A **293**, 1 (2005).
12. V. M. Akhemedov, and S. H. Al-Khowaiter, Catal. Rev. **49**, 33 (2007).
13. C. Bouchy, G. Hastoy, E. Guillon, and J. A. Martens, Oil Gas Sci. Technol. **64**, 91 (2009).
14. M. Guisnet, Catal. Today **218**, 123 (2013).
15. P. Maki-Arvela, T. A. Kaka-khel, M. Azkaar, et al., Catalysts **8**, 534 (2018).
16. W. Wang, C.-J. Liu, and W. Wu, Catal. Sci. Technol. **9**, 4162 (2019).
17. K.-C. Park and S.-K. Ihm, Appl. Catal., A **203**, 201 (2000).
18. A. Soualah, J. L. Lembreton, L. Pinard, et al., Appl. Catal., A **336**, 23 (2008).
19. F. M. Mota, C. Bouchy, E. Guillon, et al., J. Catal. **301**, 20 (2013).
20. W. Souverijns, J. A. Martens, G. F. Froment and P. A. Jacobs, J. Catal. **174**, 177 (1988).
21. J. Weitkamp, ChemCatChem. **4**, 292 (2012).
22. J. W. Thybaut, I. R. Choudhury, J. F. Denayer, et al.,Top. Catal. **52**, 1251 (2009.
23. A. Astafan, Y. Pouilloux, J. Patarin, et al., New J. Chem. **40**, 4335 (2016).
24. Y. Chen, S. Liu, H. K. Zhang, et al., J. Catal. **361**, 177 (2018).
25. P. Niu, H. Xi, J. Ren, et al., Catal. Sci. Technol. **7**, 5055 (2017).
26. Y. Bi, G. Xia, W. Huang, and H. Nie, RSC Adv. **5**, 99201 (2015).
27. X. Wu, M. Qiu, X. Chen, et al., New J. Chem. **42**, 111 (2018).
28. K. P. de Jong, J. Zecevic, H. Friedrich, et al., Angew. Chem., Int. Ed. Engl. **49**, 10074 (2010).
29. J. A. Martens, D. Verboekend, K. Thomas, et al., Catal. Today **218–219**, 135 (2013).
30. Y. Chen, C. Li, X. Chen, et al., Microporous Mesoporous Mater. **268**, 216 (2018).
31. R. Kenmogne, A. Finiels, C. Cammarano, et al., J. Catal. **329**, 348 (2015).
32. H. Song, Z. Liu, W. Xing, et al., Appl. Petrochem. Res. **4**, 401 (2014).
33. Y. Goto, Y. Fukushima, P. Ratu, et al., J. Porous Mater. **9**, 43 (2002).
34. I. I. Ivanova, A. S. Kuznetsov, V. V. Yuschenko, and E.E. Knyazeva, Pure Appl. Chem. **76**, 1647 (2004).
35. S. Inagaki, M. Ogura, T. Inami, et al., Microporous Mesoporous Mater. **74**, 163 (2004).
36. V. V. Ordomsky, V. Y. Murzin, Yu. V. Monakhova, et al., Microporous Mesoporous Mater. **105**, 101(2007).

37. J. Y. Ying and J. Garcıa-Martınez, US Patent No. 7,589,041 (2009).
38. J. Garcia-Martinez, M. Johnson, J. Valla, et al., Catal. Sci. Technol. **2**, 987 (2012).
39. M. O. Kazakov, K A. Nadeina, I. G. Danilova, et al., Catal. Today, **305**, 117 (2018).
40. R. Chal, T. Cacciaguerra, S. van Donk, and C. Gerardin, Chem. Commun. **46**, 7840 (2010).
41. R. Chal, C. Gerardin, M. Bulut, and S. van Donk, ChemCatChem. **3**, 67 (2011).
42. F. Kleitz, S. H. Choi, and R. Ryoo, Chem. Comm. **17**, 2136 (2003).
43. N. Calin, A. Galarneau, T. Cacciaguerra, et al., C. R. Chim. **13**, 199 (2010).
44. D. Desplantier-Giscard, A. Galarneau, F. Di Renzo and F. Fajula, Stud. Surf. Sci. Catal. **135**, 1105 (2001).
45. A. Galarneau, M. Nader, F. Guenneau, et al., J. Phys. Chem. B, **111**, 8268 (2007).
46. A. Galarneau, M. F. Driole, C. Petitto, et al., Microporous Mesoporous Mater. **83**, 172 (2005).
47. P. Iengo, M. Di Serio, A. Sorrentino, et al., Appl. Catal., A **167**, 85 (1998).
48. Z. Luan, M. Hartmann, D. Zhao, et al., Chem. Mater. **11**, 1621 (1999).
49. R. D. Andrei, M. I. Popa, F. Fajula, and V. Hulea, J. Catal. **323**, 76 (2015).
50. A. Galarneau, D. Desplantier, R. Dutartre, and F. Di Renzo, Microporous Mesoporous Mater. **27**, 297 (1999).
51. A. Galarneau, F. Villemot, J. Rodriguez, et al., Langmuir **30**, 13266 (2014).
52. P. I. Ravikovitc and A.V. Neimark, Langmuir **18**, 9830 (2002).
53. D. Mehlhorn, J. Rodriguez, T. Cacciaguerra, et al., Langmuir, **34**, 11414 (2018).
54. I. I. Ivanova and E. E. Knyazeva, Chem. Soc. Rev. **42**, 3671 (2013).
55. D. Verboekend, M. Milina, S. Mitchell, and J. Perez-Ramirez, J. Cryst. Growth Des. **13**, 5025 (2013).
56. D. Verboekend, N. Nuttens, R. Locus, et al., Chem. Soc. Rev. **45**, 3331 (2016).
57. C. Angell and M. Howell, J. Phys. Chem. **73**, 2551 (1969).
58. G. Eaton, A. Pena-Nunez, and M. Symons, J. Chem. Soc., Faraday Trans. **84**, 2181 (1988).
59. A. S. Medin, V. Yu. Borovkov, V. B. Kazansky, et al., Zeolites **10**, 668 (1990).
60. A. G. Pelmenschikov, R. A. van Santen, J. Janchen, and E. Meijerl, J. Phys. Chem. **97**, 11071 (1993).
61. S. Jolly, J. Saussey, and J. C. Lavalley, J. Mol. Catal. **86**, 401 (1994).
62. C. Travers, N. Essayem, M. Delage, and S. Quelen, Catal. Today **65**, 355 (2001).
63. H. I. Coonradt and W. E. Garwood, Ind. Eng. Chem. Process Des. Dev. **3**, 38(1964).
64. J. Weitkamp, *ACS Symposium Series*, vol. 20: *Hydrocracking and Hydrotreating*, Ed. by J. W. Ward (American Chemical Society, Washington, DC, 1975), p. 1.
65. Z. Adem. F. Guenneau, M. A. Springuel-Huet. et al., J. Phys. Chem. C **116**, 13749 (2012).
66. A. Galarneau, F. Guenneau, A. Gedeon, et al., J. Phys. Chem. C **120**, 1562 (2016).
67. A. Galarneau, J. Iapichella, D. Brunel, et al., J. Sep. Sci. **29**, 844 (2006).
68. J. J. van Deemter, F. J. Zuiderweg, and A. Klinkenberg, Chem. Eng. Sci. **5**, 271 (1956).
69. V. Wernert, R. Bouchet, and R. Denoyel, Anal. Chem. **82**, 2668 (2010).
70. A. Galarneau, A. Sachse, B. Said, et al., C. R. Chim. **19**, 231 (2016).
71. E. M. Renkin, J. Gen. Physiol. **38**, 225 (1954).
72. V. R. Choudhary and L. K. Doraiswamy, Ind. Eng. Chem. Prod. Res. Dev. **10**, 218 (1971).
73. E. N. Fuller, P. D. Schettler, and J. C. Giddings, Ind. Eng. Chem. **58**, 18 (1966).
74. S. J. Reich, A. Svidrytski, D. Hlushkou, et al., Ind. Eng. Chem. Res. **57**, 3031 (2018).
75. D. Peralta, G. Chaplais, A. Simon-Masseron, et al., Ind. Eng. Chem. Res. **51**, 4692 (2012).